Geophys. J. Int. (2009) **179,** 1133–1147 doi: 10.1111/j.1365-246X.2009.04331.x

High-resolution 3-D *P*-wave model of the Alpine crust

T. Diehl,[1]* S. Husen,[2] E. Kissling[1] and N. Deichmann[2]

[1]*Institute of Geophysics, Swiss Federal Institute of Technology, ETH Zürich,* CH-8092, *Switzerland. E-mail: tdiehl@ldeo.columbia.edu*
[2]*Swiss Seismological Service, Swiss Federal Institute of Technology, ETH Zürich,* CH-8092, *Switzerland*

Accepted 2009 July 9. Received 2009 July 9; in original form 2008 December 26

SUMMARY

The 3-D *P*-wave velocity structure of the Alpine crust has been determined from local earthquake tomography using a set of high-quality traveltime data. The application of an algorithm combining accurate phase picking with an automated quality assessment allowed the repicking of first arriving *P*-phases from the original seismograms. The quality and quantity of the repicked phase data used in this study allows the 3-D imaging of large parts of the Alpine lithosphere between 0 and 60 km depth. Our model represents a major improvement in terms of reliability and resolution compared to any previous regional tomographic studies of the Alpine crust. First-order anomalies like crust–mantle boundary (Moho) and the Ivrea body in the Western Alps are well resolved and in good agreement with previous studies. In addition, several (consistent) small-scale anomalies are visible in the tomographic image. A clear continuation of the lower European crust beneath the Adriatic Moho in the Central Alps is not observed in our results. The absence of such a signature may indicate the eclogitization of the subducted European lower crust in the Central Alps. In agreement with previous results, the additional analysis of focal depths in our new 3-D *P*-wave model shows that all studied earthquakes in the northern foreland have occurred within the European crust. Waveforms and focal depths suggest that at least one of the analysed events south of the Alps is located in the Adriatic mantle.

Key words: Seismicity and tectonics; Body waves; Seismic tomography; Crustal structure; Europe.

1 INTRODUCTION

The Alpine arc results from continental collision between plates or microplates of Eurasian, African and Iberian origin. The orogen reveals substantial differences between Western, Central and Eastern Alps in terms of crustal and upper-mantle structure. Based on controlled-source seismic reflection and refraction profiles (see e.g. Roure *et al.* 1990; Blundell *et al.* 1992; Pfiffner *et al.* 1997; Transalp Working Group 2002) several large-scale geophysical–geological transects of the Alpine crust were recently compiled (Schmid & Kissling 2000; Schmid *et al.* 2004). The locations of the most prominent transects (ECORS-CROP, NFP-20 West, NFP-20 East/EGT and TRANSALP) are indicated in the tectonic sketch map of Fig. 1.

In the Western Alps the European Moho dips eastwards and continental European lithosphere is subducted east to SE beneath the Adriatic microplate as revealed by high-resolution teleseismic tomography of Lippitsch *et al.* (2003). The Ivrea body located at the western end of the Po plain (Fig. 1) acted as a buttress in the collision process of the European and Adriatic plates and caused the backthrusting and doubling of the European lower crust under the Western Alps (Schmid & Kissling 2000).

In the Central Alps the structure of the lower-crustal wedge is reversed. Adriatic lower crust indents the European middle crust as described by Ye *et al.* (1995) and Schmid *et al.* (1996). According to models of Schmid *et al.* (1996) and Kissling *et al.* (2006) lower European crust and European lithosphere are subducted southward beneath the Adriatic Plate.

The upper-mantle structure in the Eastern Alps derived from teleseismic tomography of Lippitsch *et al.* (2003) indicates a change in the subduction regime between Central and Eastern Alps in the realm of the Tauern Window (Fig. 1). The subducted lower lithosphere in the Eastern Alps is part of the Adriatic lithosphere and dips NNE beneath the European Plate. In addition, differences in seismicity are observed between Central and Western Alps as described by Deichmann & Baer (1990), Sue *et al.* (1999) and Schmid & Kissling (2000). The lower-crustal wedge beneath the Central Alps appears aseismic whereas the lower-crustal wedge is seismically active beneath the Western Alps.

The seismic velocity structure of the lower crust and across the lithosphere–asthenosphere boundary represents a key parameter to

*Now at: Lamont-Doherty Earth Observatory, Columbia University, Palisades, NY, USA.

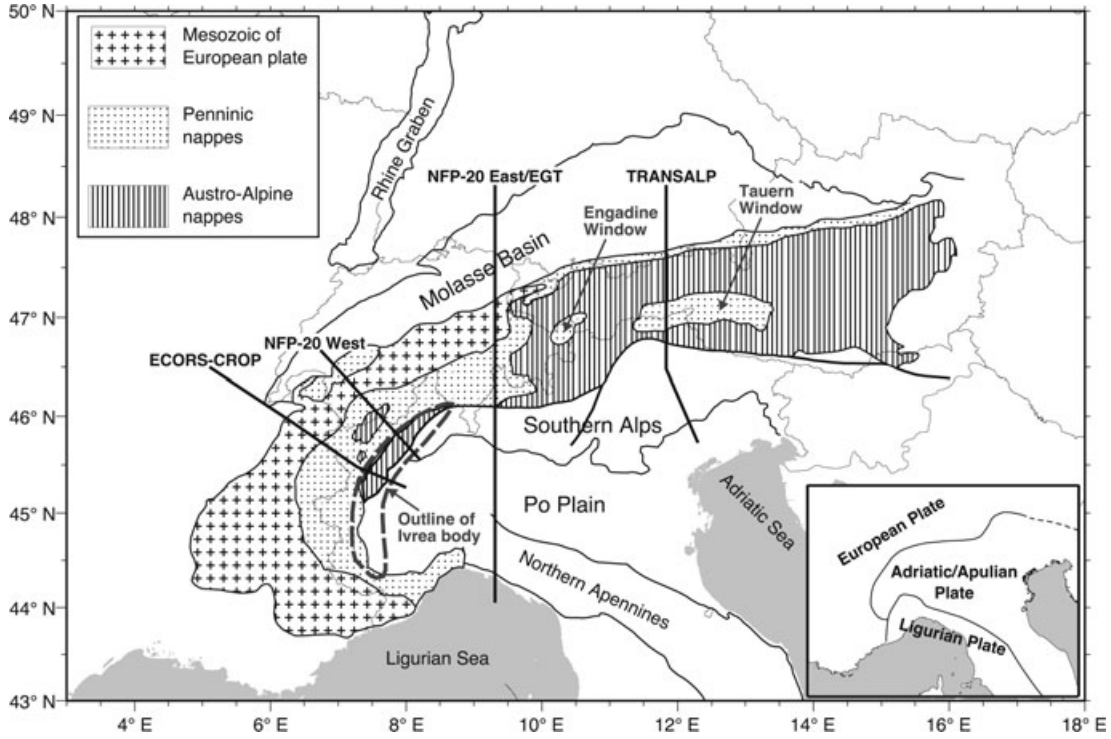

Figure 1. Tectonic sketch map of the Alpine region (modified from Carpena & Caby 1984) with locations of four crustal geophysical transects ECORS-CROP, NFP-20 West, NFP-20 East (EGT) and TRANSALP. The grey dashed contour outlines the Ivrea geophysical body.

integrate these differences into improved tectonic models. Independent models of *P*- and *S*-wave velocities can provide unique information on composition and physical state of the lithosphere (fluid content, temperature, etc.), since they allow the comparison with petrological measurements. Existing models of the Alpine crust as summarized, for example, in Schmid & Kissling (2000), Schmid *et al.* (2004) and Kissling *et al.* (2006) are mainly based on results from Controlled Source Seismology (CSS). In terms of seismic velocities, these models are poorly resolved in the depth ranges of the lower crust. Likewise, teleseismic tomography is not appropriate to resolve crustal structure due to the subvertical incidence of rays. In addition, teleseismic usually provides only relative velocity models.

Local Earthquake Tomography (LET) can be used to derive 3-D velocity images of the lithosphere with a spatial resolution up to a few tens of kilometres. Recent tomographic studies in the Alps, however, were restricted to image mostly the upper crust due to the limited aperture of the seismic network used (e.g. Solarino *et al.* 1997b; Eva *et al.* 2001; Paul *et al.* 2001; Husen *et al.* 2003). Furthermore, the resolution of existing models often suffers from low data quality, especially if routine phase data was merged from several networks (e.g. Solarino *et al.* 1997a). The impact of a high-quality data set on the resolution of the tomographic image was demonstrated by Diehl *et al.* (2009b). Recent developments in phase picking algorithms (e.g. Aldersons 2004) allow for automated repicking of large waveform data sets with a high degree of consistency. These new tools automatically assign an observation weight to each phase to quantify the uncertainty of the timing. Di Stefano *et al.* (2006) applied such a procedure to the Italian national network and improved on existing regional 3-D models for the lithosphere system beneath Italy (Di Stefano *et al.* 2009). A similar automated approach was used by Diehl *et al.* (2009b), who repicked *P*-phase data of local earthquakes in the greater Alpine region.

In this paper, we present a consistent 3-D *P*-wave velocity model of the Alpine lithosphere derived from the inversion of the high-quality phase data set of Diehl *et al.* (2009b). The focus of this study is on the structure of the Alpine lower crust and the suture zone regions, in particular. First-order anomalies like crust–mantle boundary (Moho) and the Ivrea body in the Western Alps are well resolved and several (consistent) small-scale anomalies are visible in the tomographic image. A clear continuation of the lower European crust beneath the Adriatic Moho in the Central Alps is not observed in our results. The absence of such a signature may indicate the eclogitization of the subducted European lower crust in the Central Alps.

2 LOCAL EARTHQUAKE DATA FROM AUTOMATED PHASE PICKING

The arrival-time data set used for local earthquake tomography was derived from automated repicking of waveform data as described in Diehl *et al.* (2009b). Waveforms from about 1500 events with $M_l \geq 2.5$ recorded between 1996 and 2007 were compiled from 13 national and regional networks. The MPX software of Aldersons (2004) was used for consistent and quality weighted repicking of first arriving *P*-phases. Our final data set comprises more than 13 000 phases from 552 well-locatable local earthquakes with a minimum number of eight observations per event and azimuthal gap $<180^\circ$. Epicentral distances of *Pg* and *Pn* phases in this data set vary between 1 and about 700 km. The resulting ray coverage and the station configuration is shown in Fig. 2, where hypocentres correspond to the location in the regional minimum 1-D model of Diehl *et al.* (2009b).

Table 1 summarizes the quality weighting scheme used for the automated picking of *P*-phases. The highest quality class 0 is

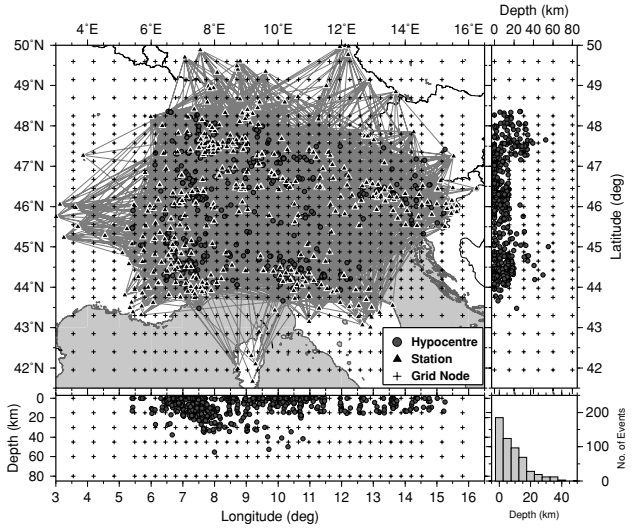

Figure 2. Ray coverage of 552 earthquakes selected for 3-D local earthquake tomography of the Alpine region. Triangles denote location of 391 seismic stations. Hypocentres (grey circles) correspond to the location in the minimum 1-D model of Diehl *et al.* (2009b). Crosses mark position of inversion grid nodes of the 3-D model.

Table 1. Weight assignments and associated uncertainty intervals used for the automated repicking of *P*-phases.

Quality class	Error ε_{qP} (s)	Weight (per cent)	# Observations
0	±0.050	100	5387
1	±0.100	50	4875
2	±0.200	25	1822
3	±0.400	12.5	1225
4	>0.400	0.0	Not considered

associated with an error interval of ±0.05 s and the lowest quality class used for 3-D tomography corresponds to an uncertainty of ±0.4 s. As demonstrated by Diehl *et al.* (2009b) the average picking error of the data set is about 0.12 s and no significant outlier picks (misidentified phases etc.) are included. The quality of this data set represents a major improvement in terms of accuracy and consistency compared to any compilation based on routine picks (Diehl *et al.* 2009b).

3 METHOD

We used the well-established SIMULPS14 software (Thurber 1983; Eberhart-Phillips 1990), extended by a full 3-D ray shooting technique (Haslinger & Kissling 2001), to invert simultaneously for hypocentre locations and 3-D *P*-wave velocity structure. Since SIMULPS14 solves the non-linear, coupled hypocentre-velocity problem by a linearized, iterative, damped, least-square approach, the solution depends on the choice of initial model (velocities, hypocentres), damping values and model parametrization (see Kissling *et al.* 2001). SIMULPS14 includes a seismic grid (representing the 3-D velocity structure) and a forward grid used by the 3-D shooting ray tracer as described by Kissling *et al.* (2001). In the seismic grid, seismic velocities are linearly interpolated between grid nodes. Since the implemented 3-D shooting ray tracer requires a cubic b-spline interpolation (Haslinger & Kissling 2001), the forward grid in SIMULPS14 is also based on a b-spline interpolation. To reduce artefacts due to interpolation-effects as much as possible,

Table 2. Initial *P*-wave velocities at nodes of 3-D gradient model. Velocities are based on minimum 1-D model of Diehl *et al.* (2009b).

Depth of grid plain (km)	v_P (km s^{-1})
0	5.50
15	6.10
30	6.60
45	7.70
60	8.00
80	8.10

the node spacing of the forward grid has to be significantly smaller than the spacing of the seismic grid (Haslinger & Kissling 2001; Kissling *et al.* 2001).

As suggested by Kissling *et al.* (1994), hypocentres and *P*-wave velocities from the minimum 1-D model of Diehl *et al.* (2009b) are used as initial values. The parametrization of the 3-D seismic grid is chosen to guarantee uniform and fair resolution in most parts of the model volume. The final parametrization is selected from several single-iteration inversions for different model parametrizations similar to the procedure described in Husen *et al.* (2003). The rather coarse grid of 25 km × 25 km (horizontal) × 15 km (vertical) for the central part of the model turned out to be the finest possible model parametrization without showing a strongly heterogeneous ray coverage. The corresponding grid nodes of the final model parametrization are indicated as crosses in Fig. 2 and the initial *P*-wave velocities are given in Table 2.

Considering the trade-off between model parametrization, minimum resolvable velocity perturbation and average data error, the chosen grid represents an appropriate parametrization to reliably resolve lower-crustal structure with at least 5 per cent velocity perturbation, assuming $v_P = 6.5$ km s^{-1}, an average ray length of $\Delta x =$ 25 km, and the given data error of 0.12 s. Furthermore, a denser forward grid of 5 km × 5 km (horizontal) × 1 km (vertical) is used to provide sufficient precision for the shooting ray tracer.

The appropriate damping value was selected empirically from a series of inversions similar to the procedure proposed by Eberhart-Phillips (1986). The trade-off curves were calculated for a large range of damping values (1, 10, 100, 1000, 10 000), and in contrast to single-loop inversions as originally suggested by Eberhart-Phillips (1986), seven iterations were performed for each damping value. The multiloop procedure provides additional information on the behaviour of trade-off curves for increasing model variance and also allows a decision on the maximum number of iterations reasonable for a chosen damping value. Data variance (as defined by eq. A1) is compared against model variance for each iteration and damping value as shown in Fig. 3(a). The preferred damping value is associated with the best compromise between data misfit reduction and model variance. As demonstrated in Fig. 3(a), the damping value 100 leads to a high data reduction with a moderate model variance for our data set and model parametrization. Lower-damping values (e.g. 10) require more iterations steps to achieve similar data reduction and lead to a large model variance (complex models). Fig. 3(b) shows the reduction of the weighted rms (as defined by eq. A2) after each iteration using an optimal damping value of 100. After iteration 5 the weighted rms is reduced by 65 per cent compared to the initial weighted rms. Further iterations lead to insignificant improvement of the data fit and therefore the inversion is terminated after five iterations (cross/square in Fig. 3).

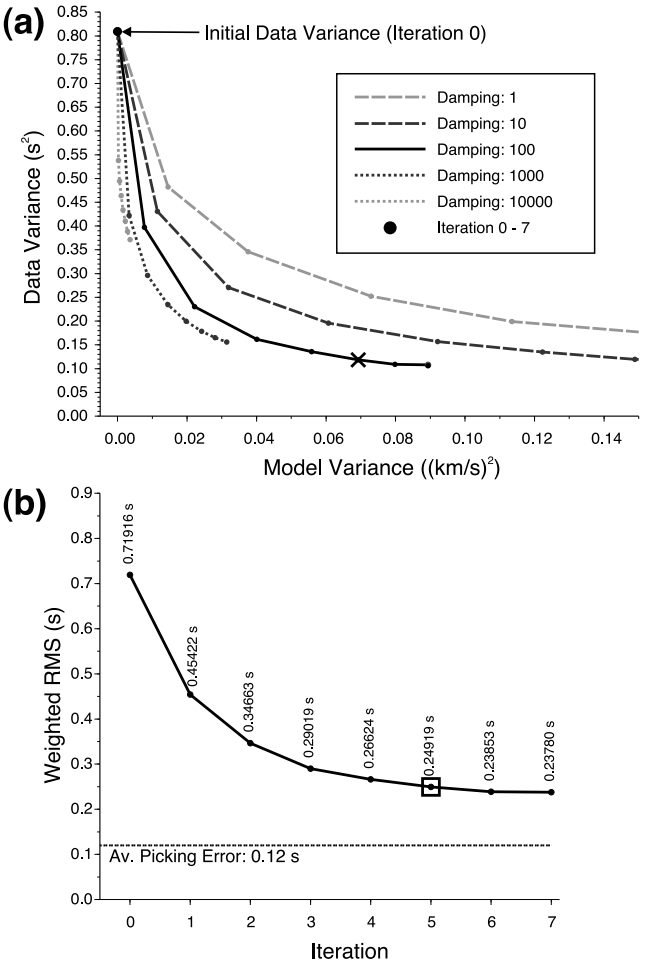

Figure 3. Trade-off curves to determine appropriate damping for inversion and the number of necessary iteration steps. (a) Data variance versus model variance. Each curve represents trade-off for different damping values over seven iterations. After five iterations, the chosen damping value of 100 (as indicated by cross) achieves an optimum misfit reduction without a strong increase in model variance. (b) Reduction of weighted rms after each iteration using a damping value of 100. After iteration five (as indicated by square) the improvement becomes insignificant.

The fact that the final rms is still remarkably larger than the average picking error of 0.12 s indicates that the inversion was not able to resolve small-scale anomalies due to the chosen relatively coarse model parametrization. A finer model parametrization would allow resolving these small-scale anomalies but ray coverage does not support this.

4 SOLUTION QUALITY

The assessment of the solution quality is a crucial component of any seismic tomography study. Areas of good resolution have to be separated from poorly or none resolved regions. In addition, the inversion process may introduce artefacts in areas of low resolution or even in areas of good resolution (Kissling *et al.* 2001). Primarily, the resolution of a specific volume depends on the associated ray coverage (density and geometric distribution of rays). Distribution of hit count or derivative weighted sum (DWS) can be used as a first-order assessment of the ray coverage. Hit count and DWS, however, are not sensitive to the geometric distribution of rays. The diagonal

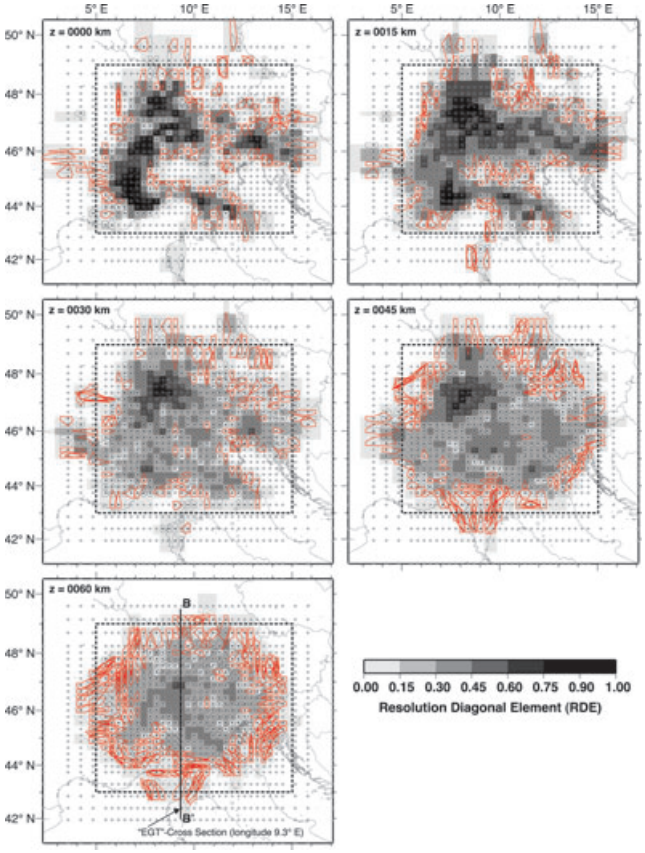

Figure 4. Diagonal elements of the resolution matrix (RDE) and resolution contours (Reyners *et al.* 1999) of the v_P solution at different depths. Crosses denote grid nodes, black dots denote grid nodes with RDE $\geq$ 0.01. The contour lines outline the area in which the values of the resolution matrix decay to 70 per cent of the value of the RDE. Black contour lines denote gridpoints with no or minor smearing, red contour lines indicate gridpoints with significant smearing. The black bold line indicates the location of the vertical cross-section of Fig. 5 and bold-dashed boxes outline the blow-up area of the final v_P model presented in the result-section.

element of the resolution matrix (RDE) provides additional information on the independence of one model parameter as described, for example, by Husen *et al.* (2000). The larger the RDE value is for one model parameter the more independent the solution is for this parameter.

Fig. 4 displays the RDE of the final 3-D v_P model for several layers between 0 and 60 km depth. For the uppermost layer the RDE is primarily dominated by station distribution and seismicity. In general, the distribution of RDE values is rather uniform, suggesting an appropriate model parametrization. However, one can observe systematically increased RDE values approximately below the territory of Switzerland. Fig. 5 displays the RDE distribution in a vertical cross-section along the southern segment of the EGT transect. The location of this depth section is indicated by the bold black line in Fig. 4. Increased RDE in a certain volume usually goes along with the presence of seismicity in or close to this volume. Furthermore, *Pn* phases lead to an increase of RDE values in the depth range between 45 and 60 km in the central part of the model.

Additional information on the solution quality can be derived from the full resolution matrix. A common diagnostic tool is the spread function (Toomey & Foulger 1989; Michelini & McEvilly 1991), which summarizes the information contained in a row of the full-resolution matrix. Thus, possible smearing (i.e. non-zero

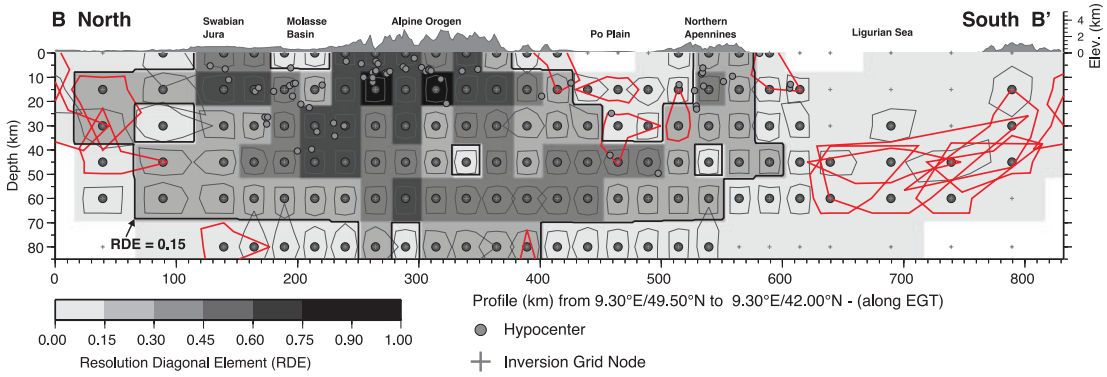

Figure 5. NS vertical cross-section of diagonal elements of the resolution matrix (RDE) and resolution contours (Reyners *et al.* 1999) of the v_P solution similar to Fig. 4. Grey dots indicate hypocentres as derived from the simultaneous 3-D inversion. Profile is situated approximately along the EGT transect (for exact location see black bold line in Fig. 4).

off-diagonal elements) will be indicated by increased spread values. However, the spread function does not show the direction of smearing. An alternative representation is proposed by Reyners *et al.* (1999), which maps the decay of the diagonal elements in each row of the resolution matrix in 2-D as smearing or resolution contours. These resolution contours visualize the orientation and the spatial bias of potential smearing. Horizontal and vertical resolution contours of the final 3-D v_P model are shown in Figs 4 and 5, respectively. The contour lines outline the area in which the values of the resolution matrix decay to 70 per cent of the value of the RDE. Black contour lines denote gridpoints with no or minor smearing, red contour lines indicate gridpoints with significant smearing (resolution contour includes a neighbouring gridpoint). Significant smearing as suggested by the resolution contours is mainly restricted to grid nodes of RDE < 0.15.

As demonstrated by Eberhart-Phillips & Reyners (1997), Kissling *et al.* (2001) and Toomey & Foulger (1989), resolution estimates based on RDE or spread values strongly depend on damping and model parametrization. Therefore, no universally applicable cut-off values are available, which define the range of acceptable RDE or spread values. A RDE threshold for the resolution assessment has to be obtained from tests with synthetic data. Checkerboard sensitivity tests (e.g. Zelt 1998) or preferable synthetic characteristic models as proposed by Haslinger *et al.* (1999) and Husen *et al.* (2000) can be used for such a RDE calibration. Following the principles of Haslinger *et al.* (1999) and Husen *et al.* (2000), we determine a RDE threshold from specifically designed synthetic tests as described in the following paragraphs and define areas of different solution qualities. Nodes associated with RDE values less than this threshold are generally considered as only fairly to poorly resolved. Well resolved parts of the model are defined as areas, where the corresponding RDE values exceed the threshold. In resolution tests with synthetic data both shape (geometry) and amplitudes of local 3-D structure are well recovered in those areas. Likewise, we define fairly resolved parts mainly as areas, where the actual RDE value is less than the threshold. Amplitudes of the recovered structures might be significantly diminished and, in addition, artefacts might be present in those areas of fair resolution. For major parts of the model, fairly resolved areas are not considered for interpretation. Poorly or unresolved parts of the model are associated with areas of DWS values less then 5 and are displayed as white areas in all tomographic images.

Fig. 6 shows the result of a sensitivity test with a synthetic checkerboard model similar to the one proposed by Husen *et al.*

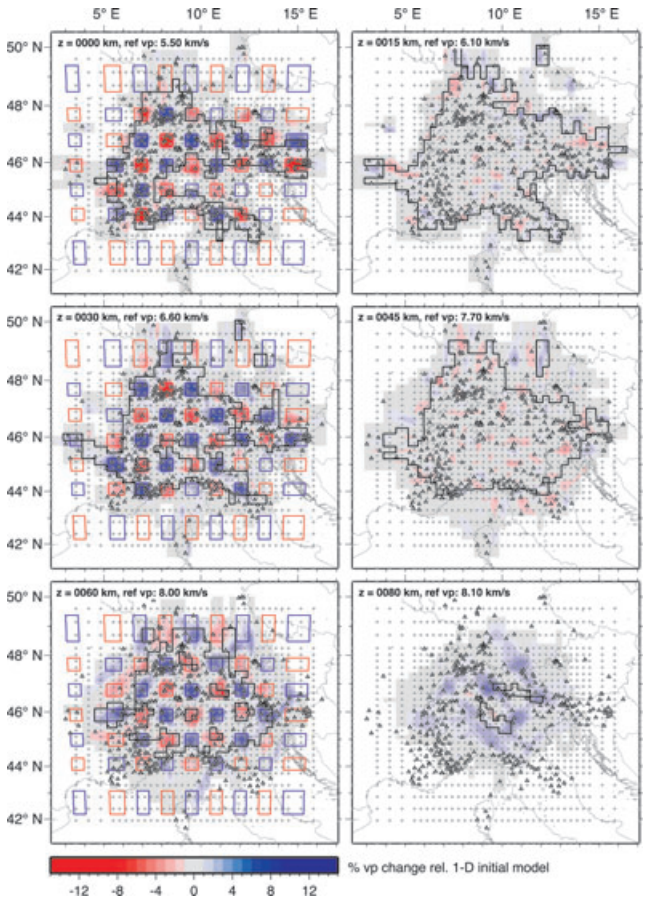

Figure 6. Sensitivity test with a checkerboard model similar to Husen *et al.* (2004). Recovered model after five iterations is shown in plane view at different depths. Alternating high (+10 per cent) and low (−10 per cent) input anomalies are indicated by blue and red rectangles, respectively. The thick black line corresponds to the RDE contour of 0.15. Crosses indicate grid nodes and triangles represent seismic stations.

(2004). To identify potential vertical leakage, only every second layer is perturbed by alternating high (+10 per cent) and low (−10 per cent) input anomalies (indicated by blue and red rectangles in Fig. 6). To identify additional horizontal smearing, a gap of two grid nodes between the input anomalies is inserted. To distinguish upward from downward leakage, the polarities of the input

anomalies are swapped for each perturbed layer. The 1-D initial velocity model as shown in Table 2 is used as background for the checkerboard model. As for all sensitivity and resolution tests in this study, synthetic traveltimes through the input model are calculated using a finite difference solution to the Eikonal equations (Podvin & Lecomte 1991) and the same source–receiver distribution as the real data set. Random noise is added to the synthetic traveltimes using an equally distributed error for each quality class. The corresponding range is defined by the error interval of the associated quality class as shown in Table 1. We use the same inversion parameters (initial model, parametrization, damping and number of iterations) for the inversion of the synthetic traveltimes as we used for the 'real' data.

The recovery of the high/low input anomalies is good for grid nodes with RDE values $\geq$0.15 as demonstrated in Fig. 6. Within the area outlined by the RDE contour of 0.15 only minor vertical and horizontal smearing is observed down to 60 km depth. The layer at 80 km depth shows significant leakage from the overlaying high velocity anomalies (Fig. 6). Although geometries of the input anomalies are well recovered by the inversion, the amplitudes are reduced by several percent, especially at deeper layers (Fig. 6). In a similar second sensitivity test (not shown here), the anomalies are placed in 15, 45 and 80 km depths and the layers at 0, 30 and 60 km remain undisturbed. The result of the inversion is comparable to the one of Fig. 6. Within the RDE contour of 0.15 the checkerboard is well resolved without showing major vertical or horizontal smearing. Below 60 km, the checkerboard cannot be recovered anymore.

The RDE value of 0.15 represents a reasonable cut-off to separate well resolved regions from fair resolution, considering the results of Figs 4–6 complemented by several additional sensitivity and specific resolution tests not shown here. Single exclaves of RDE values $\geq$0.15, however, are not considered for interpretation.

4.1 Resolution of lower crust and alpine Moho

The continuation of lower European crust beneath the Adriatic mantle wedge, as proposed in models of, for example, Schmid & Kissling (2000), is poorly documented by the available CSS data. On the other hand, temperature fields derived from kinematic modelling predict eclogitization of the subducted lower crust at a depth of 55–60 km in the Central Alps (Bousquet *et al.* 1997). Therefore, the specific resolution test shown in Fig. 7 was designed to estimate the potential recovery of geometry and amplitudes of anomalies in the range of the suture between European and Adriatic lower crust in the Central Alps. The input anomalies of the synthetic models in Fig. 7 are extended in east–west direction parallel to the strike of the Central and Eastern Alps and are placed at 45 km depth. The NS vertical cross-section of Fig. 7 is located along the EGT transect (similar to Fig. 5) and cut the input anomalies perpendicularly. Amplitudes of the synthetic anomalies with respect to the background model of Table 2 are −10 per cent (Fig. 7a) and +10 per cent (Fig. 7b). The location of the input anomalies are indicated by yellow rectangles.

The geometry of the low-velocity anomaly is well recovered by the inversion (Fig. 7a) and the vertical leakage is minor. The amplitude, however, is only partly recovered and for the major part it is diminished by more than 40 per cent (from initial anomaly of 10 per cent to recovered anomaly of 6 per cent). The recovery of the high-velocity anomaly denotes significant vertical leakage, especially towards greater depths (Fig. 7b). The upward leakage can

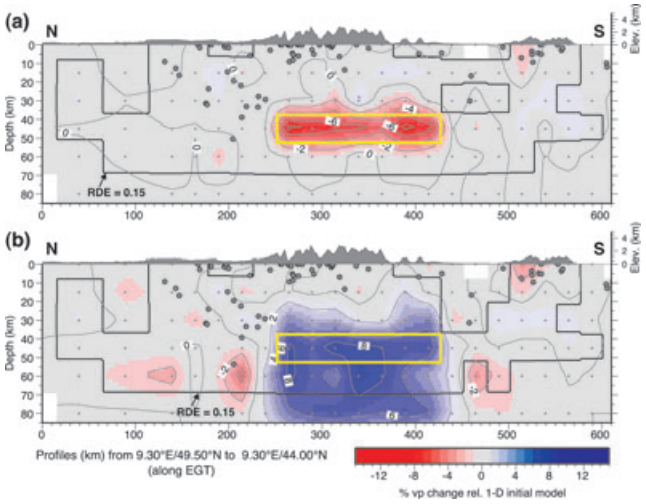

Figure 7. Assessment of resolution in the region of the expected suture between European and Adriatic lower crust below the Central Alps. NS vertical cross-section through synthetic model along EGT transect. Input anomalies are extended in EW-direction. (a) Low input anomaly (−10 per cent). (b) High input anomaly (+10 per cent). Location of input anomalies are indicated by yellow rectangles, respectively. Contour lines denote percentage v_P change with respect to initial 1-D model.

partly be identified by increased resolution contours, the downward leakage is indicated neither by spread nor by resolution contours, due to the focusing effect of the high-velocity anomaly and the low degree of 'cross-firing' of *Pn* phases in this region.

This example illustrates clearly the necessity of specific resolution tests for the assessment of the solution quality in 3-D tomography. Unmodified European crust subducted beneath the Adriatic mantle should be imaged as a low-velocity anomaly by our data set. The resolution of an eclogitized European lower crust will be rather difficult, since v_P of eclogite is expected to be comparable or even higher than v_P of the surrounding peridotite mantle rocks (e.g. Holbrook *et al.* 1992) and in this case upward and downward leakage has to be considered as demonstrated in Fig. 7(b).

Since the Alpine region shows a strong 3-D Moho topography (see e.g. Waldhauser *et al.* 1998; Lombardi *et al.* 2008), its potential resolution with local earthquake tomography is examined in an additional synthetic test. Unlike CSS refraction and reflection methods, local earthquake tomography resolves seismic velocities averaged within a volume, which is defined by the model parametrization. Therefore, sharp and well-defined seismic discontinuities like the Moho are imaged as velocity gradients in local earthquake tomography. Depending on the model parametrization, the associated velocity gradient is more or less broadened. This effect has to be taken into account for interpretation of lower-crustal velocities derived from local earthquake tomography as demonstrated in Figs 8(a)–(c).

For a synthetic test we interpolated the velocities from the Alpine crustal model of Waldhauser *et al.* (2002), which is mainly based on CSS data, on a dense grid of 5 km × 5 km (horizontal) × 2 km (vertical) nodes. Fig. 8(a) represents a vertical cross-section through the interpolated synthetic model along the EGT transect. The Moho is defined by a sharp velocity gradient in the range of 6.5–8.0 km s^{-1}. The dense grid is used to calculate synthetic traveltimes using the same source–receiver configuration as the 'real' data set, similar to previous sensitivity and resolution tests. After adding random noise, synthetic traveltimes are inverted with the same coarse model

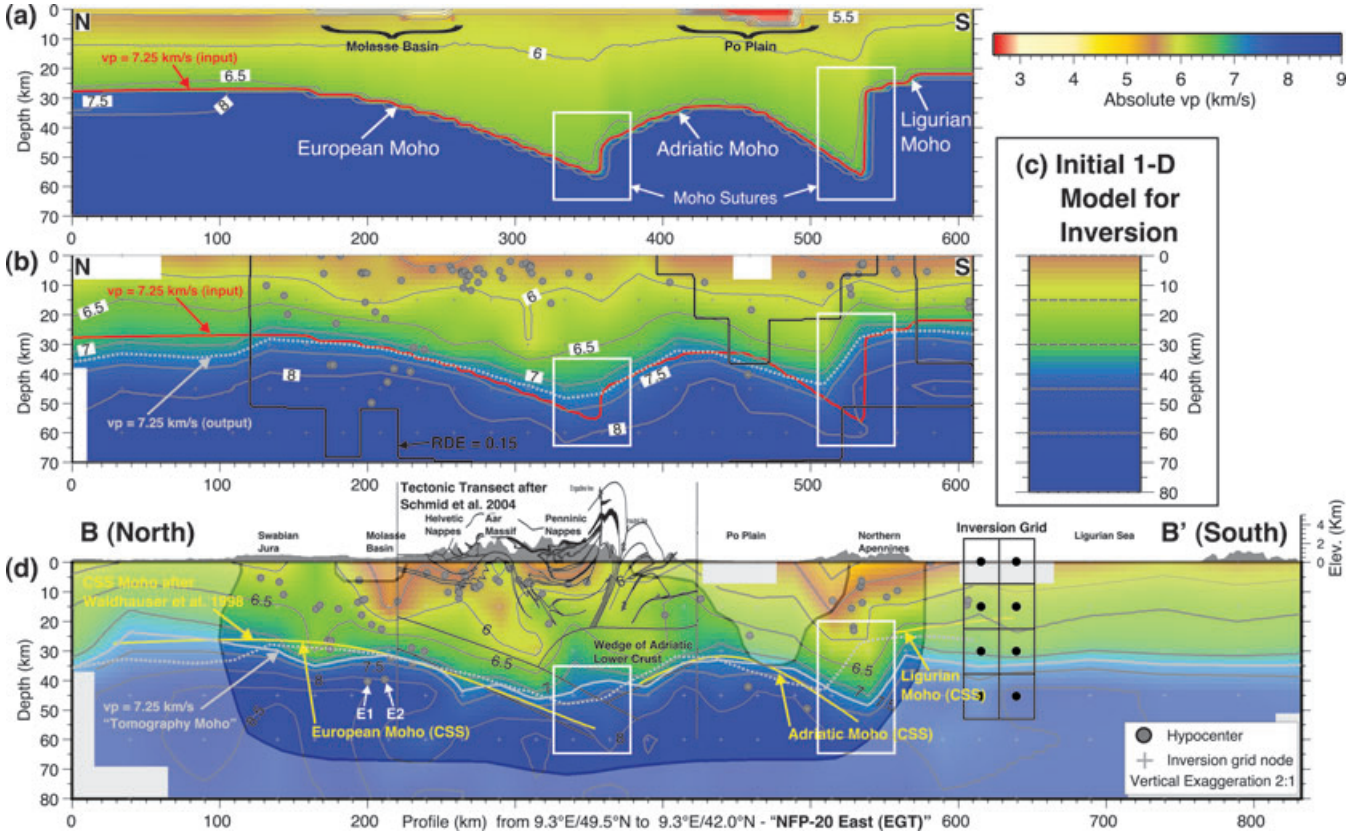

Figure 8. Resolution test and tomographic result as cross-sections along the NFP-20 East/EGT transect (see Fig. 4 for location). (a) Crustal model of Waldhauser *et al.* (2002) used to calculate synthetic traveltimes (dense model parametrization). (b) Recovered model after inversion of synthetic traveltimes with coarse parametrization. Sharp Moho-offsets (regions outlined by white rectangles) are smoothed out in the recovered model. (c) Initial 1-D model used for all 3-D inversions. (d) Final inversion result of 'real' data set. Fairly and poorly resolved areas are masked. Black lines represent tectonic transect after Schmid *et al.* (2004). Position of CSS Mohos after Waldhauser *et al.* (1998) is indicated by solid yellow line. The suture between European and Adriatic Moho is smoothed out similar to recovered synthetic model, the offset towards Ligurian Moho seems further south in the 'real' data. Projected hypocentres (grey dots) are located within ±50 km distance off the profile. Focal depths of events labelled as E1 and E2 are discussed in Section 6. Vertical exaggeration for all cross sections is 2:1.

parametrization, initial velocities and inversion parameters as used for the 'real' data.

The result of the inversion is shown in Fig. 8(b). Well resolved parts are outlined by the RDE = 0.15 contour line. Compared to the steep velocity gradient defining the Moho in the input model of Fig. 8(a), the output of the inversion denotes an obviously flatter gradient, indicated by the less dense velocity contour lines between 6.5 and 8.0 km s^{-1}. This broadening of the velocity gradient is mainly caused by the coarse parametrization of our model. Furthermore, the initial 1-D model (Fig. 8c) used for the inversion might not be the optimum choice, since it does not represent the minimum 1-D model of the CSS input model (higher velocities in the upper crust compared to CSS model).

Although the $v_P = 6.0$ km s^{-1} contour line indicates some vertical leakage problems (e.g. at 200 and 310 km), it seems not affected by the Moho topography. From this we conclude that velocities between 6.5 and 8.0 km s^{-1} are mainly associated with the Moho gradient in our model parametrization. On the other side, we observe a very good agreement between the $v_P = 7.25$ km s^{-1} contour line of the input model (solid red line in Figs 8a and b) and the $v_P = 7.25$ km s^{-1} contour line of the inversion result (dashed light grey line in Fig. 8b). Therefore, we define the $v_P = 7.25$ km s^{-1} contour line as the 'tomography' Moho in our model. Moho offsets (European/Adriatic and Adriatic/Ligurian) as indicated by kinks in the CSS model (outlined by white rectangles in Fig. 8a) are smoothed out in the recovered model (Fig. 8b).

Fig. 8(d) shows the result from the inversion of the 'real' data set as vertical cross-section along the same EGT transect (for location see Fig. 4). Fairly and poorly resolved areas are masked. Tectonic transect after Schmid *et al.* (2004) is represented by black lines and positions of CSS Mohos after Waldhauser *et al.* (1998) are indicated by solid yellow lines. Solid light grey line denotes the $v_P = 7.25$ km s^{-1} contour (tomography Moho) as derived from the 'real' data set, dashed light grey line corresponds to $v_P = 7.25$ km s^{-1} contour from the inversion of the synthetic data (same as in Fig. 8b). In general, a rather good agreement is observed between tomographic and CSS Moho. Southward dipping of the European Moho, up-doming of the Adriatic Moho and the offset between Adriatic and Ligurian Moho are clearly visible. Furthermore, the $v_P = 7.25$ km s^{-1} contour predicted by the synthetic model (dashed light grey line in Figs 8b and d) agrees very well with the tomography Moho of the 'real' data (solid light grey line in Fig. 8d). Although the 'real' data indicates slightly higher velocities in the suture zone between European and Adriatic lower crust, it shows a smoothed offset similar to the recovered synthetic model of Fig. 8(b). Therefore, the existence of a kink or offset in the range of the suture zone between European and Adriatic Moho, as present in the model of Waldhauser *et al.* (2002) (Fig. 8a), cannot be excluded.

The offset towards the Ligurian Moho seems to be located further to the south in the 'real' data. The structure of the lower crust will be discussed in detail in Section 6.

5 3-D TOMOGRAPHIC MODEL OF THE ALPINE CRUST

Fig. 9 shows the tomographic result of the 3-D v_P model as slices at different depths. The v_P velocity structure is shown as percentage change relative to the 1-D initial reference model. As shown before, perturbations $\geq$5 per cent are reliably resolved with our data. Bold black contours include well resolved regions. Areas outside these contours are associated with low resolution or are not resolved at all. These outlines are mainly based on the RDE = 0.15 contour and, in addition, results of sensitivity and resolution tests are considered for the definition of the solution quality as described in the previous section. Yellow/black dashed contours in Fig. 9 outline major tectonic units such as the Alpine orogen, the Apennines mountains, sedimentary basins (Molasse basin, Po plain) and external massifs in the northern Alpine foreland (Black-Forest, Vosges Mountains).

Due to the large vertical node spacing of our model, the layer at $z = 0$ km (Fig. 9) is dominated by near-surface and shallow upper-crustal structures. Increased v_P, as indicated by bluish colours, is observed throughout the Western Alps, where the uppermost crust is dominated by the crystalline basement (Fig. 9, 0 km). In addition, high v_P can be found in the southeastern Alps probably associated with the occurrence of compact limestones in this area. Further regions of increased v_P are the northeastern Apennines mountains as well as the southern Black-Forest. Reduced velocities as indicated by reddish colours are mainly associated with sedimentary deposits and basins such as the southern Rhine Graben, the Molasse basin and the Po plain. Although the latter two are mostly within the fairly resolved parts of the model, the reduced velocities in those areas are consistent with the local geology. Furthermore, our sensitivity tests (Fig. 6) indicate proper damping and model parametrization with no artefacts introduced in those areas of low resolution. Actual velocities in the basins, however, could be even lower considering the result of our sensitivity tests (Fig. 6).

The upper to mid crust (Fig. 9, 15 km depth) is dominated by the high-velocity anomaly of the Ivrea body in the Western Alps. West and southwest of the Ivrea body, a region of reduced v_P is observed. Furthermore, low velocities below the Apennines are identified, which can be associated with Po sediments overthrust by the Apennines mountains.

Besides these first-order anomalies, several small-scale features can be observed such as the high-velocity anomaly north of the Lago Maggiore in southern Switzerland (marked as 'T' in Fig. 9), whose location agrees very well with the Ticino-anomaly present in the gravity model of Kissling (1984). Another striking high-velocity anomaly is located in the range of the Engadine window (marked as 'E' in Fig. 9) in the border region between Austria, Italy and Switzerland.

Reduced velocities in the mid to lower-crust section (Fig. 9, 30 km depth) are mainly associated with the crustal root of the Alps and the northern Apennines. On the other hand, significantly increased velocities indicate the transition to upper-mantle velocities in regions of crust of average normal thickness of about 30 km (e.g. northern foreland, Ligurian Sea). The signature of the Ivrea body is still observable at this this depth range as well as the small-scale Ticino anomaly.

Likewise, lower velocities at 45.0 km depth (Fig. 9) clearly reveal the thickening of the crust beneath the Alpine and Apennine orogens. Increased v_P correlates with upper-mantle velocities of European, Adriatic and Ligurian plates. The signature of the Ivrea body is not observed anymore.

The zones of slightly reduced velocities at 60 km depth (Fig. 9) correlate largely with the deepest parts of the crustal root as reported in the CSS model of Waldhauser *et al.* (1998) and in the receiver function study of Lombardi *et al.* (2008). Based on the resolution test shown in Fig. 7, however, further interpretation have to take into account possible reduction of low-velocity and vertical leakage of high-velocity anomalies at this this depth range.

6 DISCUSSION

Fig. 10 shows further vertical cross-sections located perpendicular to the strike of the Alpine orogen as indicated in the map view. Profiles AA′, DD′ and EE′ are located along prominent geophysical–geological transects also marked in Fig. 1. Like in Fig. 8(d) the tomographic Moho is indicated by solid light grey lines and locations of the CSS Mohos after Waldhauser *et al.* (1998) are indicated by solid yellow lines (Fig. 10). As demonstrated by Diehl *et al.* (2009b), the general topography of the tomographic Moho (v_P = 7.25 km s^{-1} iso-surface), is in good agreement with the CSS model of Waldhauser *et al.* (1998) and with the recent receiver function study of Lombardi *et al.* (2008). In the Western and Central Alps the European Moho dips towards southeast to south. The suture between the European and Adriatic lower crust is of asymmetric nature mainly caused by the Ivrea body in the Western Alps (profile EE′, DD′, CC′ BB′ in Figs 10 and 8d).

Although Behm *et al.* (2007) recently compiled a Moho map for the Eastern Alps, the transition between Central Alps and Eastern Alps is still less well documented by CSS data. Profile AA′ (Fig. 10) along the TRANSALP transect suggests a rather symmetric Moho topography, although a major part of the European Moho is outside the well resolved volume. Compared to our result, the location of the European Moho on the TRANSALP transect of Schmid *et al.* (2004) seems to be too deep. The structure of the Ivrea body in the Western Alps is well resolved from its northeastern end down to its southern end. Profile EE′ in Fig. 10 represents a cross-section along the ECORS-CROP transect. The location of the high-velocity anomaly in our model agrees well with the tomography study of Solarino *et al.* (1997a) superimposed for comparison in Fig. 10 (vertical cross-section as published in Schmid & Kissling 2000). Similar to the result of Solarino *et al.* (1997a) a pronounced low-velocity anomaly is present northwest of the Ivrea body (EE′ in Fig. 10), probably associated with European upper crust wedged into the suture zone. Likewise, a low-velocity anomaly is observed in the range of the expected doubled lower crust (Schmid & Kissling 2000) along the NFP-20 West transect (profile DD′ in Fig. 10). Profile CC′ in Fig. 10 marks the northeastern end of the Ivrea body.

In the Central Alps reduced *P*-wave velocities between 5.5 and 6.0 km s^{-1} reach almost to the suture between the European lower crust and the Adriatic lower crustal indenter in 25 km depth (profile BB′ in Fig. 8d), indicating thickening of the upper European crust. However, vertical leakage as demonstrated in Fig. 8(b) cannot be entirely excluded in this part of the model. Likewise, the low-velocity zone in the upper crust below the Molasse basin is most probably stretched by vertical leakage or inappropriate model parametrization (Fig. 8d). Helvetic nappes and Penninic nappes are characterized by *P*-wave velocities around 5.5 km s^{-1} in the upper

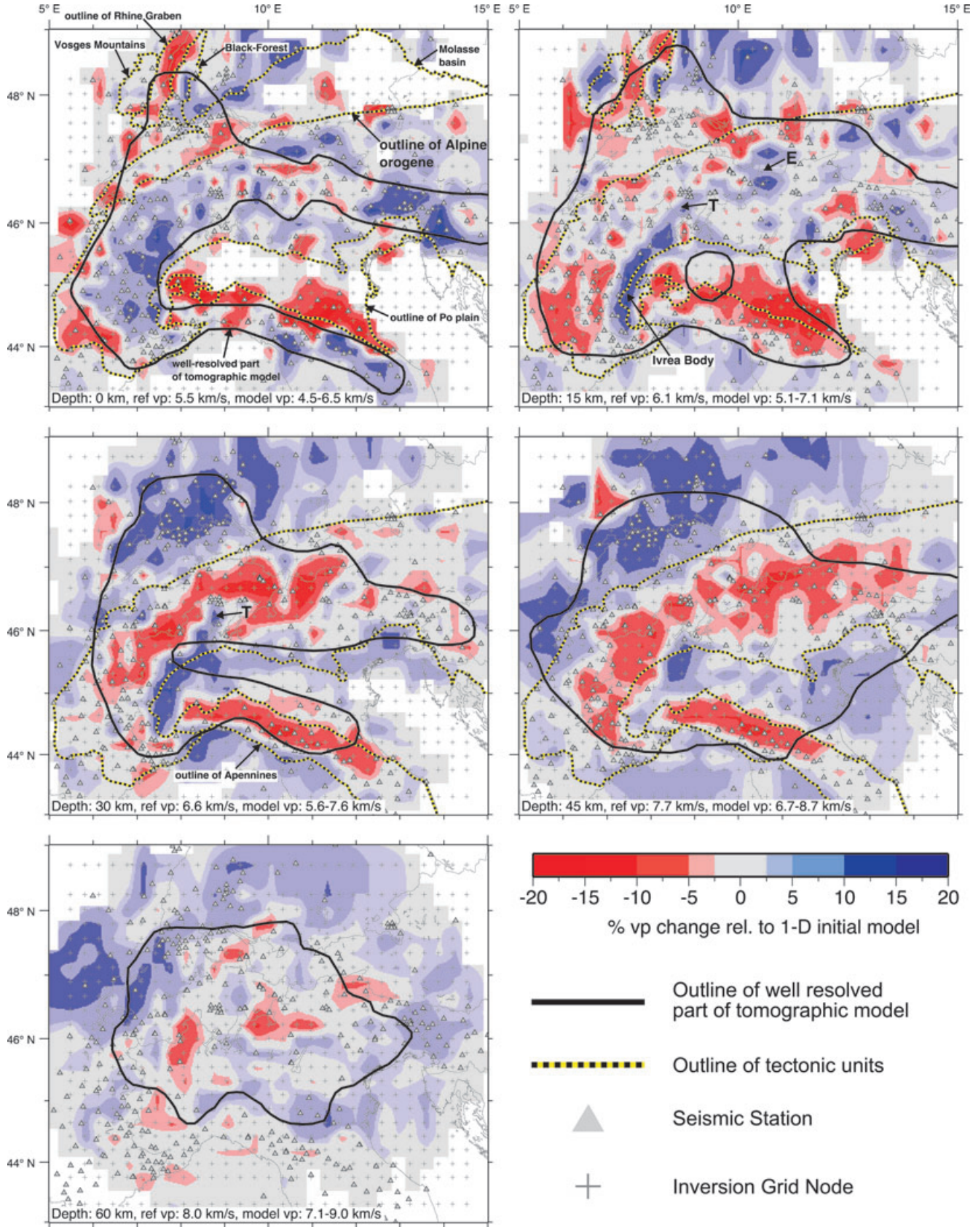

Figure 9. Tomographic results of 3-D v_P model (blow-up as outlined by dashed boxes in Fig. 4). Results are in horizontal cross-sections at different depths as indicated. The v_P velocity structure is shown as percentage change relative to the 1-D initial reference model. Bold black contours include well resolved regions. Areas outside these contours are associated with fair or poor resolution or are not resolved at all. Major tectonic units are outlined as indicated. 'E' and 'T' mark positions of small-scale anomalies as discussed in the text. Grey triangles indicate seismic stations used for tomographic inversion.

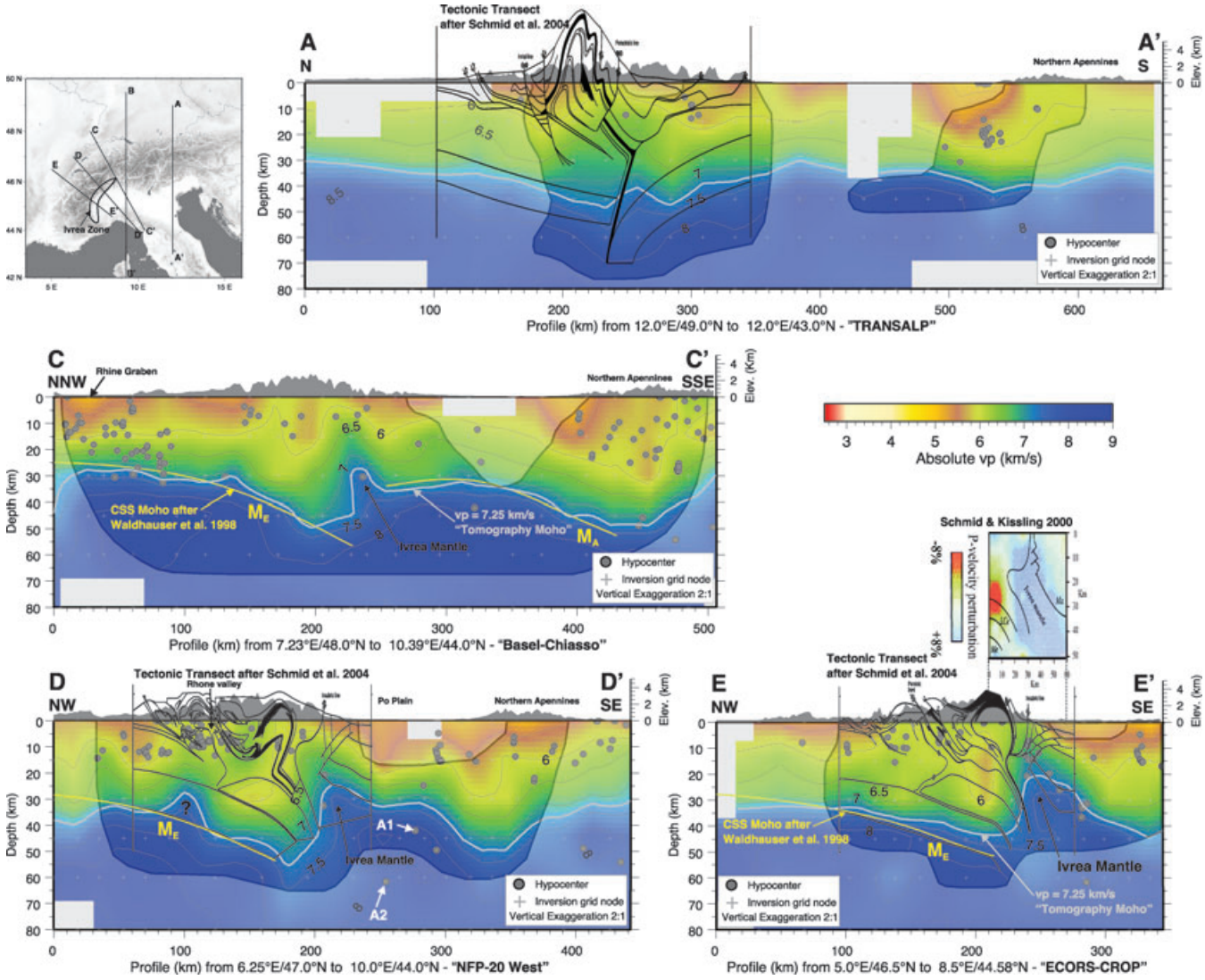

Figure 10. Final *P*-wave velocity model. Vertical cross-sections perpendicular to the strike of the Alpine orogen as indicated in map view. Profiles AA′, DD′ and EE′ are located along prominent geophysical-geological transects. Fairly and poorly resolved areas of the tomographic model are masked. Tectonic interpretations of Schmid *et al.* (2004) are indicated by black lines. M_E denotes European Moho, M_A denotes Adriatic Moho as derived from the CSS model of Waldhauser *et al.* (1998). Projected hypocentres (grey dots) are located within ±50 km distance off the profile. Profile BB′ is shown in Fig. 8(d). Focal depths of events labelled as A1 and A2 in profile DD′ are discussed in Section 6.

crust. Realms of Helvetic nappes and Penninic nappes are separated by a zone of slightly increased v_P located in the area of the Aar Massif (around km 290 on profile BB′ in Fig. 8d). These observations are in very good agreement with the velocity model of Ye *et al.* (1995) derived from seismic refraction data of the EGT transect.

6.1 Structure of the lower crust in the central Alps

A continuation of the lower European crust beneath the Adriatic Moho is not visible in our tomographic image of Fig. 8(d). The absence of the lower European crust beneath the Adriatic mantle wedge might be an indication for eclogitization of subducted lower-crustal material or, alternatively, extrusion of European lower crust. To check the hypothesis of existing subducted (unmodified) European lower crust beneath the Adriatic mantle wedge, an additional resolution test was performed as shown in Figs 11(a)–(c). Similar to Fig. 8(a) the synthetic input model for our test is based on the CSS model of Waldhauser *et al.* (2002), however, in this case a coarser grid was used for interpolation. Unmodified lower European crust ($v_P = 6.5$ km s^{-1}) is extrapolated beneath the Adriatic mantle wedge assuming a constant dip and thickness of the subducted lower crust as indicated by dashed lines in Fig. 11(a).

The result of the inversion of synthetic traveltimes for this model is shown in Fig. 11(b). The solid red line denotes the $v_P = 7.25$ km s^{-1} contour of the input model (Figs 11a and b) and the $v_P = 7.25$ km s^{-1} contour recovered by the inversion is indicated by the dashed light grey line (Figs 11b and c). As expected from the previous resolution test in Fig. 7(a), recovered amplitudes of low-velocity anomalies in the lower crust are significantly attenuated compared to their input. The comparison of Figs 11(b) with 8(b) leads to the conclusion that the presence of subducted lower crust is primarily indicated by the kink in the 7.25 km s^{-1} contour (around km 360 on profile) and the downward deflection of the 8.0 km s^{-1} contour (solid yellow line) below the Adriatic mantle wedge. In

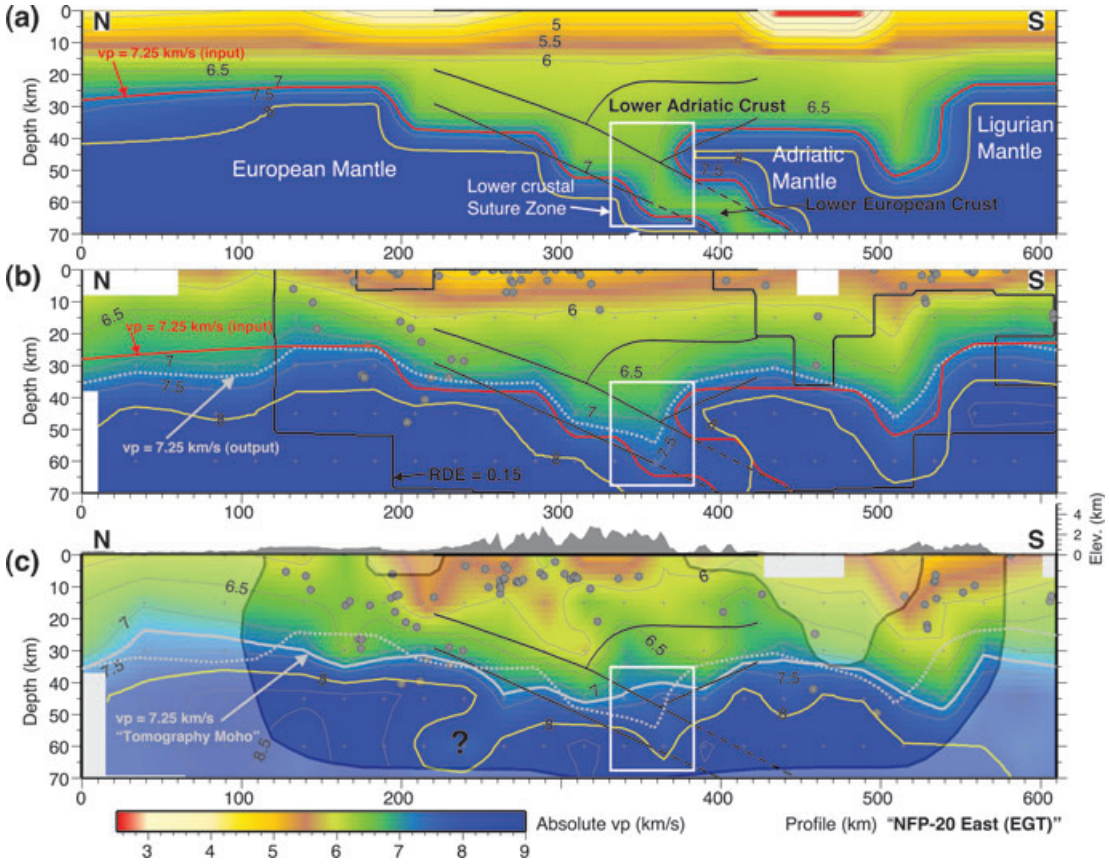

Figure 11. Resolution assessment for lower-crustal subduction in the Central Alps. (a) Synthetic model based on CSS crustal model with European lower crust subducted below Adriatic microplate. (b) Recovered model after inversion of synthetic traveltimes. In contrast to Fig. 8b, subducted European lower crust is indicated by a kink of the 7.25 km s^{-1} contour (dashed light grey line) around km 360 on the profile and the strong downward deflection of the 8.0 km s^{-1} contour (solid yellow line) below the Adriatic mantle wedge. (c) Inversion result of 'real' data set identical to Fig. 8(d). Neither a kink of the 7.25 km s^{-1} contour (solid light grey line) nor a deflection of the 8.0 km s^{-1} contour (solid yellow line) is observed below the Adriatic mantle wedge. The lack of such signature might be explained by a thinner subducted crustal layer not resolved with the chosen parametrization, by mineral transition due to metamorphic processes (eclogitization), or by extrusion of lower European crust.

the 'real' data (Fig. 11c) neither a kink of the 7.25 km s^{-1} contour nor a deflection of the 8.0 km s^{-1} contour (solid yellow line) is observed below the Adriatic mantle wedge. The cause of the low-velocity anomaly visible in the European mantle at a depth of about 60 km (downward deflection of 8.0 km s^{-1} contour), labelled by a question-mark in Fig. 11(c), is probably associated with a numerical artefact, caused by the inhomogeneous resolution in this part of the model (see Fig. 5). The presence of unmodified European lower crust beneath the Adriatic mantle wedge, as proposed in the model of Fig. 11(a), should lead to an observable signature in the tomographic image. The lack of such signature might be explained by a thinner subducted crustal layer not resolved with our parametrization, by mineral transition due to metamorphic processes, or by lower-crustal extrusion.

Phase-transition of material in the lower continental crust from and to eclogite presumably plays an important role in continental collision and the tectonic evolution of orogenic belts as described, for example, by Ahrens & Schubert (1975), Richardson & England (1979), Dewey *et al.* (1993), Austrheim *et al.* (1997) and Le Pichon *et al.* (1997). Eclogitization of subducted continental crust below the Alpine orogen is proposed by Butler (1986) as driving force for post-collisional subduction of European crust and subsidence of the Po plain region. Consequently, the imaged geophysical Moho in the Alps represents a mixture between compositional-boundary (crust–mantle) and metamorphic phase-change (granulite, amphibolite/eclogite) in this model. Based on results of seismic refraction and reflection surveys, Laubscher (1990) postulated similarly a new Moho in the suture between European and Adriatic plates, which formed by eclogitization of subducted crustal material. From kinematic modelling eclogitization of subducted lower crust is predicted at a depth of 55–60 km in the Central Alps (Bousquet *et al.* 1997). In a similar study, Henry *et al.* (1997) proposed the absence of eclogitization above 75 km within the underthrust Indian lower crust, which leads to crustal-like densities down to 75 km below the Himalayas. They argue that the differences in densities of subducted lower crust might cause the differences in the average elevation between Alps and Himalayas.

Extrusion might represent an alternative explanation for the observed absence of European lower crust beneath the Adriatic mantle. During continental collision, the entire European crust might have been forced to detach (from the underlaying mantle) and deform, creating a crustal wedge as described, for example, by Beaumont *et al.* (1996). Such mechanism, however, would require extrusion and stacking of large volumes of lower European crust considering the estimated post-collisional crustal shortening of 120–170 km in the Western and Central Alps during the past 35 Myr (e.g. Schmid & Kissling 2000; Lippitsch *et al.* 2003). Hence, the model of extruded lower European crust is—at least partly—inconsistent with

the Adriatic lower crustal indentation (Adriatic indenter) proposed by Schmid *et al.* (1996). Pfiffner *et al.* (2000) simulated Alpine collision tectonics for different material properties (strength of upper/lower crust, mantle, suture material, etc.) using a simplified 2-D finite element method. European crust is subducted in all of their geodynamic models, which suggests that lower-crustal extrusion requires rather complex collision models. In addition, material balance estimates and palaeogeographic reconstructions indicate that large parts of the continental crust must have disappeared into the mantle (Laubscher 1988, 1990; Le Pichon *et al.* 1988).

Altogether, extrusion alone appears to be rather unlikely as sole explanation for the observed absence of subducted European lower crust, however, the combination of both mechanisms might have occurred in the Central Alps. Extruded, stacked lower crust might remain in areas, where the European Moho is identified by the CSS data (around km 320 to km 360 on profile BB′ in Fig. 8d) and eclogitization of lower crust is likely to be present below the Adriatic mantle wedge (around km 360 to km 420 on profile BB′ in Fig. 8d). In such model, the location of the postulated extruded lower European crust would overlap with realms hitherto associated with the Adriatic indenter (Schmid *et al.* 1996). Upward bending of the $v_P = 6.5\ \mathrm{km\,s^{-1}}$ contour can be observed in the tomographic image in this region (around km 340 on profile BB′ in Fig. 8d). Since this feature is not present in the synthetic model of Fig. 8(b), the increase in v_P in this part of the model can be associated either with the Adriatic indenter, extruded European lower crust, or a stack of both.

6.2 Focal depth distributions in the greater Alpine region

The distribution of earthquake focal depths within the continental lithosphere provides important information on its mechanical strength and rheology as demonstrated, for example, by Chen & Molnar (1983), Maggi *et al.* (2000) or Jackson (2002). Since then, the issue of a seismogenic continental mantle and its implications for continental geodynamics are intensively discussed (see e.g. Priestley *et al.* 2007, and references therein). Although the lower European crust in the northern Alpine foreland is known to be seismically active, no evidence exists for earthquakes in the European mantle in this area (Deichmann *et al.* 2000). The presence of fluids might play a key role for the occurrence of the lower-crustal seismicity as proposed by Deichmann (1992). In contrast, there are several indications for a seismogenic Adriatic upper mantle in northwestern Italy (e.g. Cattaneo *et al.* 1999).

As visible in the cross-sections of Figs 8(d) and (10) the simultaneous inversion yields a couple of hypocentres which are apparently located within the upper European (e.g. events E1, E2 in Fig. 8d) and Adriatic (e.g. events A1, A2 in Fig. 10) mantle. To clarify if these events really occurred in the continental mantle we examined events, which were located below the CSS (minimum uncertainty ±3 km, Waldhauser *et al.* 1998) and the tomographic Moho. In total, we found 11 events apparently situated in the European (seven events, all in the northern foreland) and Adriatic (four events, all in northwestern Italy) mantle.

To assess the uncertainty of the hypocentre solutions in further detail, we relocated all 11 events in our new 3-D *P*-wave model using the NonLinLoc package of Lomax *et al.* (2000). This approach provides a probabilistic solution to the earthquake location problem, including information on uncertainty and resolution. Considering the relocated hypocentres and the corresponding uncertainties of focal and Moho depths, nine of the events could also be located just above the Moho (Table 3). Only two events in northwestern Italy (A1, A2 in Fig. 10) suggest locations in the Adriatic mantle.

In a final check we produced velocity reduced record sections for each event similar to the procedures described for example in Deichmann (1987), Deichmann & Rybach (1989), or Diehl *et al.* (2009b). Events located above the Moho can be identified by the presence of both *PmP* and *Pn* phases in these record sections. Events located in the mantle are characterized by the lack of *PmP* phases. The additional assessment of velocity reduced record sections showed that all apparent mantle-events in the northern foreland (including events E1, E2 in Fig. 8d) have occurred in the lower European crust, only few kilometres above the Moho. These results are in agreement with the results of Deichmann *et al.* (1998, 2004, 2006) and Baer *et al.* (2001, 2003, 2005) who used 2-D ray tracing techniques and similar record sections to determine focal depths for the annual seismicity reports of the Swiss Seismological Service. The same conclusion holds for the events in northwestern Italy with the exception of event A1 and A2. Waveforms and focal depths suggest that event A1 (few kilometres southwest of Milan) occurred in the Adriatic mantle. Due to its large uncertainty in focal depth, a final decision on the origin of event A2 is not possible.

Finally, it should be mentioned that the influence of focal depth uncertainties of single events on the tomographic velocity model is insignificant, since hypocentre parameters are separated from velocity parameters in the simultaneous inversion. Therefore, the resolution estimate of velocities is sufficient for the entire model and independent from the location-accuracy of a single earthquake.

Table 3. Apparent upper-mantle events relocated in the 3-D model using the NonLinLoc package.

Date	Time	Lat. N	Lon. E	Z_F (km)	Z_M (km)	Final Origin in
1997/09/02	00:30:52.82	47.599	7.824	29 ± 02	27	Eur. crust
2000/04/21	04:12:11.17	45.021	8.764	51 ± 10	44	Adr. crust
2000/09/16	22:04:05.56	45.028	8.016	67 ± 13	43	Adr. mantle? (A2)
2002/01/10	19:27:25.78	47.565	9.052	31 ± 02	30	Eur. crust
2002/05/17	07:19:39.78	47.675	8.476	29 ± 03	28	Eur. crust
2002/07/06	14:09:56.85	47.711	9.700	36 ± 11	31	Eur. crust (E1)
2003/08/24	12:43:40.61	47.805	7.971	30 ± 02	26	Eur. crust
2004/04/18	03:21:05.03	47.594	9.678	40 ± 04	33	Eur. crust (E2)
2005/05/12	01:38:05.39	47.296	7.636	30 ± 02	29	Eur. crust
2005/11/20	10:48:59.95	45.378	9.058	40 ± 03	33	Adr. mantle (A1)
2007/04/02	09:10:33.28	45.777	8.300	33 ± 03	27	Adr. crust

Notes: Focal depths are indicated by Z_F. Moho depths Z_M are taken from the CSS-model of Waldhauser *et al.* (1998). Final origins are based on Z_F, Z_M, corresponding uncertainties and waveform analysis. Eur., European; Adr., Adriatic. Labels in parentheses denote events discussed in the text.

7 CONCLUDING REMARKS

The quality and quantity of the automatically repicked arrival-time data used in this study allows the 3-D imaging of large parts of the Alpine lithosphere. The new *P*-wave model represents a major improvement over existing models in terms of reliability and resolution of the resulting tomographic image (Diehl *et al.* 2009b). First-order anomalies such as the crustal roots of the Alps and the northern Apennines are clearly resolved. Several additional small-scale features like the Ticino-anomaly northwest of the Ivrea body are visible in the tomographic image.

Different sensitivity and resolution tests were performed to assess the solution quality of the resulting velocity model in detail. Synthetic tests using a realistic 3-D crustal model were performed to assess the resolution of the crust–mantle boundary (Moho). It is shown, that the general Moho topography can be recovered even with a rather coarse model parametrization.

The Alpine Moho topography derived from local earthquake tomography agrees very well with existing models from CSS methods and receiver function studies. Steep gradients are found in the Western Alps and a wider trough in combination with a rather symmetric suture between European and Adriatic crust is observed in the Eastern Alps.

The Ivrea body is clearly resolved in our model and its position and structure agrees very well with previous studies (e.g. Solarino *et al.* 1997a; Schmid & Kissling 2000). Several low-velocity anomalies are imaged in the upper and mid crust northwest of the Ivrea zone as well as in the Central Alps. These structures are probably associated with wedges of upper-crustal material present north of the Insubric line.

Continuation of the lower European crust beneath the Adriatic mantle wedge in the Central Alps is not visible in our tomographic image. By comparing results of the synthetic modelling with the velocity model derived from our 'real' data set in Fig. 11, we can exclude the subduction model for the Central Alps presented in Fig. 11(a). The presence of unmodified European lower crust beneath the Adriatic mantle wedge should lead to an observable signature in the tomographic image. The lack of such signature might be explained by a thinner subducted crustal layer not resolved with our parametrization, by eclogitization of the subducted lower crust, or by extrusion of lower European crust. Considering the average picking error and the vertical leakage associated with high-velocity anomalies as observed in Fig. 7(b), the discrimination of an eclogitized lower crust from the surrounding mantle would not be possible, since v_P of both rock types is expected to be about 8 km s^{-1}. In agreement with the results of Bousquet *et al.* (1997) $v_P = 8.0$ km s^{-1} is reached in a depth of 55 to 60 km in the suture between lower European crust and Adriatic mantle wedge (Fig. 11c). However, due to the described effects of model parametrization and leakage in this part of the model, the uncertainties in terms of absolute velocities are rather high. Extrusion might represent an alternative explanation for the observed absence of European lower crust beneath the Adriatic mantle. Results of material balance estimates, paleogeographic reconstructions, geodynamical modelling, and CSS-surveys suggest that extrusion of the complete lower European crust is very unlikely. The combination of both mechanisms, however, might be conceivable: extrusion of lower European crust in the realm associated with the Adriatic indenter and eclogitization of subducted lower European crust beneath the Adriatic mantle wedge. Finally, the detailed assessment of focal depths within our new 3-D *P*-wave model demonstrated that uncertainties of model and hypocentres have to be taken into account prior to any rheological interpretation of the continental lithosphere. In agreement with previous results, the additional analysis of waveforms showed clearly that all apparent mantle-events in the northern foreland have occurred in the lower European crust. Waveforms and focal depths suggest that at least one event is most likely located in the Adriatic mantle south of the Alps.

Further enhancement of data coverage is necessary to overcome the relatively coarse model parametrization and to improve the spatial resolution in the upper and mid crust in future studies. A denser spacing of stations in some regions of the Alps, common data exchange procedures between networks, and further improvement of the picking performance of automatic algorithms as described by Diehl *et al.* (2009b) are required to fill the gaps in the ray distribution present in Fig. 4.

Finally, information on *S*-wave velocities are necessary for further interpretations of composition and rheology of the Alpine lithosphere. Recently, a similar approach was developed for automated picking of *S*-wave arrival-times at local to regional scales (Diehl 2008; Diehl *et al.* 2009a). Although accuracy and quality classification are comparable to manually picked *S*-waves, the coverage of the corresponding data set is mainly limited by the quality of available waveform data in the Alpine region. The reliable identification of first arriving *S*-waves requires three-component (3C) recordings of high quality (broad dynamic range of sensors and transmission systems to avoid clipped amplitudes, etc.). In addition, regional *S*-phases such as *Sn* are usually very weak in amplitude and therefore difficult to identify and to pick. The average uncertainties of such *Sn* phases are several times larger compared to *Pn* phases. Beyond epicentral distances of 150 km, only few *Sn* phases can be picked reliably (manually as well as automatically). At the moment, the distribution of hypocentres and high-quality 3C-stations allow only local *S*-wave studies in certain parts of the Alps.

ACKNOWLEDGMENTS

We are grateful to the responsibles of the following networks who provided us with digital recordings and bulletin data: Geophysical Observatory Fürstenfeldbruck (Ludwig-Maximilians-University, Munich), GERESS (Hannover), GRSN/SZGRF (Erlangen), INGV/MEDNET (Rome), Landes-Erdbebendienst (Freiburg i. B.), OGS/CRS (Udine/Trieste), RENASS (Strasbourg), RSNI/DipTeris (Genova), SED (Zurich), SISMALP (Grenoble), SNRS (Ljubljana), TGRS (Nice), ZAMG (Vienna). The corresponding waveform data is available online as 'Special Data set' at ORFEUS (http://www.orfeus-eu.org).

Most of the plots were generated using the Generic Mapping Tool by Wessel & Smith (1995). We thank J. Trampert and one anonymous reviewer whose thoughtful remarks and recommendations greatly improved the manuscript. This research was supported by the Swiss National Fund grant 200021-103698.

REFERENCES

Ahrens, T.J. & Schubert, G., 1975. Rapid formation of eclogite in a slightly wet mantle, *Earth planet. Sci. Lett.,* **27,** 90–94.

Aldersons, F., 2004. Toward three-dimensional crustal structure of the Dead Sea region from local earthquake tomography, *PhD thesis*, Tel Aviv University, Israel.

Austrheim, H., Erambert, M. & Engvik, A.K., 1997. Processing of the crust in the root of the Caledonian continental collision zone: the role of eclogitization, *Tectonophysics,* **273,** 129–153.

Baer, M. *et al.*, 2001. Earthquakes in Switzerland and surrounding regions during 2000, *Eclogae Geol. Helv.,* **94**(2), 253–264.

Baer, M. *et al.*, 2003. Earthquakes in Switzerland and surrounding regions during 2002, *Eclogae Geol. Helv.,* **96**(2), 313–324.

Baer, M. *et al.*, 2005. Earthquakes in Switzerland and surrounding regions during 2004, *Eclogae Geol. Helv.,* **98**(3), 407–418.

Beaumont, C., Ellis, S., Hamilton, J. & Fullsack, P., 1996. Mechanical model for subduction-collision tectonics of Alpine-type compressional orogens, *Geology,* **24,** 675–678.

Behm, M., Brückl, E., Chwatal, W. & Thybo, H., 2007. Application of stacking and inversion techniques to three-dimensional wide-angle reflection and refraction seismic data of the Eastern Alps, *Geophys. J. Int.,* **170,** 275–298.

Blundell, D., Freeman, R. & Mueller, S., 1992. *A Continent Revealed, the European Geotraverse,* Cambridge University Press, New York.

Bousquet, R., Goffé, B., Henry, P., Le Pichon, X. & Chopin, C., 1997. Kinematic, thermal and petrological model of the Central Alps: Lepontine metamorphism in the upper crust and eclogitisation of the lower crust, *Tectonophysics,* **273,** 105–127.

Butler, R.W.H., 1986. Thrust tectonics, deep structure and crustal subduction in the Alps and Himalayas, *J. Geol. Soc., Lond.,* **143,** 857–873.

Carpena, J. & Caby, R., 1984. Fission-track evidence for late Triassic oceanic crust in the French occidental Alps, *Geology,* **12,** 108–111.

Cattaneo, M., Augliera, P., Parolai, S. & Spallarossa, D., 1999. Anomalously deep earthquakes in northwestern Italy, *J. Seismol.,* **3,** 421–435.

Chen, W.-P. & Molnar, P., 1983. Focal depths of intracontinental and intraplate earthquakes and their implications for the thermal and mechanical properties of the lithosphere, *J. geophys. Res.,* **88,** 4183–4214.

Deichmann, N., 1987. Focal depths of earthquakes in northern Switzerland, *Ann. Geophys.,* **5b,** 395–402.

Deichmann, N., 1992. Structural and rheological implications of lower-crustal earthquakes below northern Switzerland, *Phys. Earth planet. Inter.,* **69,** 270–280.

Deichmann, N. & Baer, M., 1990. Earthquakes focal depths below the Alps and northern Alpine foreland of Switzerland, in *The European Geotraverse: Integrative Studies,* pp. 277–288, eds Freeman, R., Giese, P. & Mueller, S., Eur. Sci. Found., Strasbourg, France.

Deichmann, N. & Rybach, L., 1989. Earthquakes and temperatures in the lower crust below the northern Alpine foreland of Switzerland, in *The Lower Crust: Properties and Processes,* Vol. 6, pp. 197–213, eds Mereu, R.F., Mueller, S. & Fountain, D.M., AGU-Monograph 51, IUGG.

Deichmann, N. *et al.*, 1998. Earthquakes in Switzerland and surrounding regions during 1997, *Eclogae Geol. Helv.,* **91**(2) 237–246.

Deichmann, N. *et al.*, 2000. Earthquakes in Switzerland and surrounding regions during 1999, *Eclogae Geol. Helv.,* **93**(3) 395–406.

Deichmann, N. *et al.*, 2004. Earthquakes in Switzerland and surrounding regions during 2003, *Eclogae Geol. Helv.,* **97**(3) 447–458.

Deichmann, N. *et al.*, 2006. Earthquakes in Switzerland and surrounding regions during 2005, *Eclogae Geol. Helv.,* **99**(3) 443–452.

Dewey, J.F., Ryan, P.D. & Andersen, T.B., 1993. Orogenic uplift and collapse, crustal thickness, fabrics and metamorphic phase changes: the role of eclogites, in *Magmatic Processes and Plate Tectonics,* Vol. 76, pp. 325–343, eds Prichard, H.M., Alabaster, T., Harris, N.B.W. & Neary, C.R., Geol. Soc. London, Spec. Publ.

Di Stefano, R., Aldersons, F., Kissling, E., Baccheschi, P., Chiarabba, C. & Giardini, D., 2006. Automatic seismic phase picking and consistent observation error assessment: application to the Italian seismicity, *Geophys. J. Int.,* **165,** 121–134.

Di Stefano, R., Kissling, E., Chiarabba, C., Amato, A. & Giardini, D., 2009. Shallow subduction beneath Italy: three-dimensional images of the Adriatic-European-Tyrrhenian lithosphere system based on high-quality *P* wave arrival times, *J. geophys. Res.,* **114,** B05305, doi:10.1029/2008JB005641.

Diehl, T., 2008. 3-D seismic velocity models of the Alpine crust from local earthquake tomography, *PhD thesis*, ETH Zurich, no. 17840.

Diehl, T., Deichmann, N., Kissling, E. & Husen, S., 2009a. Automatic S-wave picker for local earthquake tomography, *Bull. seism. Soc. Am.,* **99,** 1906–1920.

Diehl, T., Kissling, E., Husen, S. & Aldersons, F., 2009b. Consistent phase picking for regional tomography models: application to the greater Alpine region, *Geophys. J. Int.,* **176,** 542–554.

Eberhart-Phillips, D., 1986. Three-dimensional velocity structure in northern California Coast Range from inversion of local earthquake arrival times, *Bull. seism. Soc. Am.,* **76,** 1025–1052.

Eberhart-Phillips, D., 1990. Three-dimensional P and S velocity structure in the Coalinga region, California, *J. geophys. Res.,* **95,** 15 343–15 363.

Eberhart-Phillips, D. & Reyners, M., 1997. Continental subduction and three-dimensional crustal structure: the northern South Island, New Zealand, *J. geophys. Res.,* **102,** 11 843–11 861.

Eva, E., Solarino, S. & Spallarossa, D., 2001. Seismicity and crustal structure beneath the western Ligurian Sea derived from local earthquake tomography, *Tectonophysics,* **339,** 495–510.

Haslinger, F. & Kissling, E., 2001. Investigating effects of 3-D ray tracing methods in local earthquake tomography, *Phys. Earth planet. Inter.,* **123,** 103–114.

Haslinger, F. *et al.*, 1999. 3-D crustal structure form local earthquake tomography around the Gulf of Arta (Ionian region, NW Greece), *Tectonophysics,* **304,** 201–218.

Henry, P., Le Pichon, X. & Goffé, B., 1997. Kinematic, thermal and petrological model of the Himalayas: constraints related to metamorphism within the underthrust Indian crust and topographic elevation, *Tectonophysics,* **273,** 31–56.

Holbrook, W.S., Mooney, W.D. & Christensen, N.I., 1992. The seismic velocity structure of the deep continental crust, in *The Continental Lower Crust,* pp. 1–43, eds Fountain, D.M., Arculus, R., & Kay, R.W., Elsevier, Amsterdam.

Husen, S., Kissling, E. & Flueh, E.R., 2000. Local earthquake tomography of shallow subduction in north Chile: a combined onshore and offshore study, *J. geophys. Res.,* **105,** 28 183–28 198.

Husen, S., Kissling, E., Deichmann, N., Wiemer, S., Giardini, D. & Baer, M., 2003. Probabelistic earthquake location in complex three-dimensional velocity models: application to Switzerland, *J. geophys. Res.,* **108,** 2077.

Husen, S., Smith, R.B. & Waite, G.P., 2004. Evidence for gas and magmatic sources beneath the Yellowstone volcanic field from seismic tomographic imaging, *J. Volc. Geotherm. Res.,* **131,** 397–410.

Jackson, J., 2002. Strength of the continental lithosphere: time to abandon the jelly sandwich? *GSA Today,* **12,** 4–10.

Kissling, E., 1984. Three-dimensional gravity model of the Northern Ivrea-Verbano zone, in *Geomagnetic and Gravimetric Studies of the Ivrea Zone,* Matér. Géol. Suisse, Géophys., Vol. 21, pp. 53–61, eds Wagner, J.J. & Mueller, S., Kümmerly & Frey, Geographischer Verlag, Bern.

Kissling, E., Ellsworth, W.L., Eberhart-Phillips, D. & Kradolfer, U., 1994. Initial reference models in local earthquake tomography, *J. geophys. Res.,* **99**(B10), 19 635–19 646.

Kissling, E., Husen, S. & Haslinger, F., 2001. Model parametrization in seismic tomography: a choice of consequence for the solution quality, *Phys. Earth planet. Inter.,* **123,** 89–101.

Kissling, E., Schmid, S.M., Lippitsch, R., Ansorge, J. & Fügenschuh, B., 2006. Lithosphere structure and tectonic evolution of the Alpine arc: new evidence from high-resolution teleseismic tomography, in *European Lithosphere Dynamics,* pp. 129–145, eds Gee, D.G. & Stephenson, R.A., Geological Society, London, Memoirs 32.

Laubscher, H., 1988. Material balance in the Alpine orogeny, *Geol. Soc. Am. Bull.,* **100,** 1313–1328.

Laubscher, H., 1990. The problem of the Moho in the Alps, *Tectonophysics,* **182,** 9–20.

Le Pichon, X., Bergerat, F. & Roulet, M.J., 1988. Plate kinematics and tectonics leading to the Alpine belt formation; a new analysis, *Geological Society of America Special Paper,* **218,** 111–131.

Le Pichon, X., Henry, P. & Goffé, B., 1997. Uplift of Tibet: from eclogites to granulites—implications for the Andean Plateau and the Variscan belt, *Tectonophysics,* **273,** 57–76.

Lippitsch, R., Kissling, E. & Ansorge, J., 2003. Upper mantle structure beneath the Alpine orogen from high-resolution teleseismic tomography, *J. geophys. Res.,* **108**(B8), 2376.

Lomax, A., Virieux, J., Volant, P. & Thierry-Berge, C., 2000. Probabilistic earthquake location in 3D and layered models, in *Advances in Seismic Event Location,* pp. 101–134, eds Thurber, C.H. & Rabinowitz, N., Kluwer, Amsterdam.

Lombardi, D., Braunmiller, J., Kissling, E. & Giardini, D., 2008. Moho depth and Poisson's ratio in the western-central Alps from receiver functions, *Geophys. J. Int.,* **173,** 249–264.

Maggi, A., Jackson, J., McKenzie, D. & Priestley, K., 2000. Earthquake focal depths, effective elastic thickness, and the strength of the continental lithosphere, *Geology,* **28,** 495–498.

Michelini, A. & McEvilly, T.V., 1991. Seismological studies at Parkfield, I, Simultaneous inversion for velocity structure and hypocenters using cubic B-splines parameterization, *Bull. seism. Soc. Am.,* **81,** 524–552.

Paul, A., Cattaneo, M., Thouvenot, F., Spallarossa, D., Béthoux, N. & Fréchet, J., 2001. A three-dimensional crustal velocity model of the southwestern Alps from local earthquake tomography, *J. geophys. Res.,* **106**(B9), 19 367–19 390.

Pfiffner, O.A., Lehner, P., Heitzmann, P., Müller, S. & Steck, A., 1997. *Deep structure of the Alps: Results of NRP20,* Birkhäuser Verlag, Basel.

Pfiffner, O.A., Ellis, S. & Beaumont, C., 2000. Collision tectonics in the Swiss Alps: insight from geodynamic modeling, *Tectonics,* **19,** 1065–1094.

Podvin, P. & Lecomte, I., 1991. Finite difference computation of travel times in very contrasted velocity models: a massively parallel approach and its associated tools, *Geophys. J. Int.,* **105,** 271–284.

Priestley, K., Jackson, J. & McKenzie, D., 2007. Lithospheric structure and deep earthquakes beneath India, the Himalaya and southern Tibet, *Geophys. J. Int.,* **172,** 345–362.

Reyners, M., Eberhart-Phillips, D. & Stuart, G., 1999. A three-dimensional image of the shallow subduction: crustal structure of the Raukumara Peninsula, New Zealand, *Geophys. J. Int.,* **137,** 873–890.

Richardson, S.W. & England, P.C., 1979. Metamorphic consequences of crustal eclogite production in overthrust orogenic zones, *Earth planet. Sci. Lett.,* **42,** 183–190.

Roure, F., Heitzmann, P. & Polino, R., 1990. Early neogene deformation beneath the Po plain, constraints on the post-collisional Alpine evolution, in *Deep Structure of the Alps,* pp. 309–322, ed. Polino, R., Memoire de la societee geologique Suisse.

Schmid, S.M. & Kissling, E., 2000. The arc of the western Alps in the light of geophysical data on deep crustal structure, *Tectonics,* **19**(1), 62–85.

Schmid, S.M., Pfiffner, O.A., Froitzheim, N., G., S. & Kissling, E., 1996. Geophysical-geological transect and tectonic evolution of the Swiss-Italian Alps, *Tectonics,* **15,** 1036–1064.

Schmid, S.M., Fügenschuh, B., Kissling, E. & Schuster, R., 2004. Tectonic map and overall architecture of the Alpine orogen, *Eclogae geol. Helv.,* **97,** 93–117.

Solarino, S., Kissling, E., Sellami, S., Smriglio, G., Thouvenot, F., Granet, M., Bonjer, K.-P. & Sleijko, D., 1997a. Compilation of a recent seismicity data base of the greater Alpine region from several seismological networks and preliminary 3D tomographic results, *Ann. di Geofis.,* **XL,** 161–174.

Solarino, S., Kissling, E., Cattaneo, M. & Eva, C., 1997b. Local earthquake tomography of the southern part of the Ivrea body, North-Western Italy, *Eclogae geol. Helv.,* **90,** 357–364.

Sue, C., Thouvenot, F., Frechet, J. & Tricart, P., 1999. Widespread extension in the core of the western Alps revealed by earthquake analysis, *J. geophys. Res.,* **104,** 25 611–25 622.

Thurber, C.H., 1983. Earthquake locations and three-dimensional crustal structure in the Coyote Lake area, central California, *J. geophys. Res.,* **88,** 8226–8236.

Toomey, D.R. & Foulger, G.R., 1989. Tomographic inversion of local earthquake data from the Hengill-Grensdalur central volcano complex, Iceland, *J. geophys. Res.,* **94,** 17 497–17 510.

Transalp Working Group, 2002. First deep seismic reflection images of the Eastern Alps reveal giant crustal wedges and transcrustal ramps, *Geophys. Res. Lett.,* **29**(10), 1452, doi:10.1029/2001GL014911.

Waldhauser, F., Kissling, E., Ansorge, J. & Mueller, S., 1998. Three-dimensional interface modelling with two-dimensional seismic data: the Alpine crust-mantle boundary, *Geophys. J. Int.,* **135,** 264–278.

Waldhauser, F., Lippitsch, R., Kissling, E. & Ansorge, J., 2002. High-resolution teleseismic tomography of upper-mantle structure using an a priori three-dimensional crustal model, *Geophys. J. Int.,* **150,** 403–414.

Wessel, P. & Smith, W.H.F., 1995. New version of the Generic Mapping Tool released, *EOS, Trans. Am. geophys. Un.,* **76,** 329.

Ye, S., Ansorge, J., Kissling, E. & Mueller, S., 1995. Crustal structure beneath the eastern Swiss Alps derived from seismic refraction data, *Tectonophysics,* **242,** 199–221.

Zelt, C.A., 1998. Lateral velocity resolution frown three-dimensional seismic refraction data, *Geophys. J. Int.,* **135,** 1101–1112.

APPENDIX A: DEFINITION OF DATA VARIANCE AND WEIGHTED RMS

The data variance shown in Fig. 3(a) is defined as

$$\text{var} = \frac{1}{wndof} \sum_{i=1}^{nobs} w_i \, \delta t_i^2, \tag{A1}$$

where *wndof* is the weighted number of degrees of freedom defined by

$$wndof = \left(\sum_{i=1}^{nobs} w_i \right) - (4 \cdot neqs) - nnode, \tag{A2}$$

where *nobs* is the total number of observations (*P*-phase picks), w_i is the weight of the *i*th-observation (between 0 and 1), *neqs* is the total number of earthquakes, *nnode* is the number of inverted velocity nodes and δt_i is the *i*th-residual between theoretical and observed traveltime.

The weighted rms shown in Fig. 3(b) is defined as

$$\text{rms}_{\text{weighted}} = \sqrt{\frac{1}{\sum_{i=1}^{nobs} w_i} \sum_{i=1}^{nobs} w_i \, \delta t_i^2}. \tag{A3}$$